Atmos. Chem. Phys. Discuss., 14, 11041–11074, 2014
www.atmos-chem-phys-discuss.net/14/11041/2014/
doi:10.5194/acpd-14-11041-2014

Atmospheric Chemistry and Physics Discussions

Observation and analysis of speciated atmospheric mercury in Shangri-la, Tibetan Plateau, China

H. Zhang[1,2], X. W. Fu[1], C.-J. Lin[1,3,4], X. Wang[1,2], and X. B Feng[1]

[1]State Key Laboratory of Environmental Geochemistry, Institute of Geochemistry, Chinese Academy of Sciences, Guiyang 550002, China
[2]University of Chinese Academy of Sciences, Beijing 100049, China
[3]Department of Civil Engineering, Lamar University, Beaumont, Texas 77710, USA
[4]College of Energy and Environment, South China University of Technology, Guangzhou 510006, China

Received: 26 March 2014 – Accepted: 11 April 2014 – Published: 5 May 2014

Correspondence to: X. B. Feng (fengxinbin@vip.skleg.cn)

Published by Copernicus Publications on behalf of the European Geosciences Union.

Abstract

This study reports the speciated concentration and the potential sources of atmospheric mercury measured at the Shangri-La Atmosphere Watch Regional Station (SAWRS), a pristine high-altitude site (3580 m a.s.l.) in Tibetan Plateau, China. The total gaseous mercury (TGM, defined as the sum of Gaseous Elemental Mercury, GEM, and gaseous oxidized mercury, GOM), GOM and particulate-bound mercury (PBM) were monitored from November 2009 to November 2010 to investigate the characteristics and atmospheric transport of mercury influenced by the Indian summer monsoon (ISM) and westerlies. The mean concentrations of TGM, PBM and GOM were $2.55 \pm 0.73\,\mathrm{ng\,m^{-3}}$, $37.78 \pm 31.35\,\mathrm{pg\,m^{-3}}$ and $7.90 \pm 7.89\,\mathrm{pg\,m^{-3}}$. A notable seasonal pattern was observed with higher TGM concentrations in the beginning and end of the ISM. High TGM concentrations were associated with the transport of dry air that carried regional anthropogenic emissions from both domestic and foreign sources. The low PBM and GOM level was attributed to the deposition and wet scavenging during the ISM period. Backward trajectory analysis of air masses associated with TGM levels suggested that both the ISM and westerlies can carry Hg emitted in Burma, Bengal bay and north India to the SAWRS.

1 Introduction

Mercury (Hg) is a persistent toxic pollutant released to the atmosphere from both anthropogenic and natural sources in different chemical and physical forms (Pirrone et al., 1996, 2001; Carpi and Lindberg, 1998). Due to the volatility in its elemental form, Hg can be transported over a long distance and enters terrestrial and aquatic ecosystems in remote area through dry and wet deposition (Johansson et al., 2001). Deposited Hg can be converted into methyl-mercury, a potent neurotoxin that accumulates in the food chain and causes severe public health concerns (Lindqvist, 1991; Sunderland et al., 2009). In the atmosphere, Hg interconverts among GEM, GOM and PBM, with

ACPD
14, 11041–11074, 2014

GEM as the predominant specie constituting > 90 % of total Hg (Iverfeldt and Lindqvist, 1986; Schroeder and Munthe, 1998). The typical background concentrations of GEM, GOM and PBM measured at remote sites are in the range of 1–4 ngm^{-3}, 5–70 pg m^{-3} and 7–100 pg m^{-3}, respectively (Iverfeldt and Lindqvist, 1986; Lin and Pehkonen, 1999; Valente et al., 2007).

Observational data of atmospheric Hg are important to understand its global biogeochemical cycling. The long-term, continuous data measured at remote sites are particularly useful because such datasets yield valuable evidence of seasonal trend and transport pattern of a given region (Li and Lee, 2014; Pirrone et al., 2010; Driscoll et al., 2013). In addition, the data give basis for constraining atmospheric models of Hg. To address the data need, there has been ongoing efforts on establishing monitoring networks, including the atmospheric mercury network (AMNet) in North America and the global mercury observation system (GMOS) (Sprovieri et al., 2013; Gay et al., 2013). However, the data at remote monitoring sites are still largely insufficient to describe the temporal and spatial variability of Hg at a global scale. Monitoring speciated Hg at remote sites is challenging due to issues related to instrumental maintenance, accessibility to the sites and other logistic limitations. To date, the availability of speciated Hg observations is inadequate for a thorough understanding of Hg chemical transport in different regions.

Shangri-La is located in the southeastern corner of Tibetan Plateau that extends from 25° to 45° N and from 70° to 105° E. The Plateau covers approximately one-quarter of the land area in Mainland China with a mean elevation of more than 4000 m above sea level. Positioned geographically between South and East Asia, the air composition in Shangri-La is potentially influenced by the two largest source regions in the world. Recently, there is an increasing number of studies highlighting large and accelerating Hg emissions in fast developing countries (Pirrone et al., 2010). China is the largest Hg emitter in the world, despite its continued effort in Hg emission reduction (Streets et al., 2005; Pacyna et al., 2006). India, with the world's fourth biggest coal reserve, is another rapidly growing economy whose Hg use and emissions have been increasing

ACPD
14, 11041–11074, 2014

over the last few decades (Sharma, 2003). Recent assessments suggested that air emissions in India are of global importance, especially to the Tibetan Plateau where the long-range transport of black soot accelerates the glacier melt (Xu et al., 2009). It has been suggested that Hg deposited on Tibetan glaciers has led to the higher Hg concentrations in the snow packs (Loewen et al., 2007; Zhang et al., 2012). In addition, Hg emissions from the biomass burning in Southeast Asia represent a significant yet uncertain regional source (Pirrone et al., 2010). In light of these perspectives, Shangri-La appears to be a strategic observational site for studying the long-range transport of Hg emitted from these sources.

In this study, we report the characteristics of the speciated atmospheric Hg at the SAWRS and analyze the potential source regions that contributed to the observed concentrations. In particular, we assess the role of the Indian Summer Monsoon (ISM) and the westerlies on the long-range transport of mercury. This study is part of the Global Mercury Observation System (GMOS, http://www.gmos.eu/), which is aimed to establish a global mercury monitoring network for ambient concentrations and deposition of mercury though ground-based observational platforms as well as oceanographic aircraft campaigns. The data within the GMOS network will provide valuable global monitoring data for modeling assessment in understanding the global biogeochemical cycling of Hg, and for establishing the global source–receptor relationship of Hg emissions. The program involves 24 partners in the world (Gay et al., 2013).

2 Materials and methods

2.1 Measurement site description

Figure 1 shows the locations of SAWRS and large Asian cities with industrial production. The SAWRS (28°01′ N, 99°44′ E, 3580 m a.s.l.) is a remote highland site located in Hengduan Mountains area of the southeast of the Tibetan Plateau. It has a cold and dry winter that lasts 5 months from late October to April before onset of the ISM. Its

ACPD
14, 11041–11074, 2014

annual average temperature is 5.1 °C. The average temperature is −1.4 °C from December to February and 12.4 °C from June to August (Table 1). The SAWRS is 30 km north of Shangri-La city. The closest large point sources are in Kunming city, capital of Yunnan province, which is ∼ 650 km northwest. Other large cities (Chengdu, Guiyang and Chongqing are east of Shangri-La. India and Bengal are west of Shangri-La and Southeast Asia is due southeast. The SAWRS is near a mountaintop and surrounded by alpine forest. The population density in Shangri-La is approximately 10 persons per square kilometer. There is no large-scale industrial activities and fossil fuel consumption in the area. Domestic biofuel burning for cooking and house heating is the main emission source, which release < 10 g km^{-2} of Hg annually.

2.2 Sampling methods and analysis

2.2.1 Measurements of atmospheric TGM, PBM and GOM

The inlet of heated Teflon sampling tubing for TGM monitoring was set up at 10 m above ground. Measurement of the TGM concentrations was performed with an automated Hg vapor analyzer Tekran Model 2537A (Schroeder et al., 1995). The instrument allows continuous measurement of TGM (GEM + GOM) in ambient air through a cycle of gold trap amalgamation, thermal desorption and detection by cold vapor atomic fluorescence spectrometry (λ = 253.7 nm). The precision, accuracy, stability of the instrument have been documented extensively (Gay et al., 2013). Tekran 2537A automatically calibrates for Hg^0 every 25 h using an internal permeation source, which provides approximately 1 pg s^{-1} of Hg^0 at 50 °C into a zero air stream. External calibration using Tekran 2505 with manual injections of known concentrations of Hg^0 were performed every 4 months. The precision is < 2 % with a detection limit < 0.1 ng m^{-3}. PBM in ambient air was removed using a 47 mm diameter Teflon filter (pore size 0.2 µm). A Teflon sampling tube with its inlet 10 m above ground was employed at the sampling site. For sampling at the reduced ambient pressure at the site, a lower sampling rate of 0.75 L min^{-1} (at

ACPD
14, 11041–11074, 2014

standard temperature and pressure, as compared to the typical 1 L min^{-1}) at sampling interval of 5 min was used during the entire campaign (Fu et al., 2012a).

A denuder-based system was used for sampling PBM and GOM. The annual denuder tubes are made of quartz with the inner wall coated with KCl for GOM sampling. An integrated elutriator/acceleration jet and a glass impactor plate capable of removing coarse particles (> 2.5 µm) were installed before the inlet of the denuder. A fresh glass impactor was replaced when finished one sampling cycle. PBM (defined as Hg associated with particles < 2.5 µm) was collected on 47 mm diameter quartz filters housed in a Teflon filter holder downstream of the denuder. Each quartz filter was used for one sampling and analysis cycle to prevent from possible deformation and contamination (Xiao et al., 1997; Landis et al., 2002; Feng et al., 2000). Both the PBM filter and denuder were positioned vertically. The inlets were located at 1.5 m above ground to prevent dust from entering. An electronic temperature-controlled heating tape was utilized to maintain the temperature of the denuder sampling train at 40–50 °C above the ambient temperature to prevent water condensation over the KCl coating and the wall loss of GOM in the sampling tube (Feng et al., 2000). The sampling flow rate (10 L min^{-1}) for both GOM and PBM was controlled by mass-flow controllers (MKS, USA) calibrated to standard atmospheric pressure (0 °C and 1013 mbar). Both PBM and GOM samples were collected every 2 h.

Analytical procedures for PBM and GOM described by Landis et al. (2002) were followed (Landis et al., 2002). After sampling, Hg contents are determined via pyrolysis followed by Tekran 2537A detection. First, the Tekran 2537A pulled Hg-free air (0.5 L min^{-1}) through the trap and denuders for two sample cycles (10 min) to confirm the zero background for ensuring no leaks in the system. Then, the trap and denuders were rapidly heated to 900 and 500 °C using a pyrolyzer for three heating cycles (15 min) to convert PBM and GOM into Hg^0, which is analyzed by the Tekran2537A. Typically, a signal of < 2 pg was observed in the third heating cycle, which is indistinguishable from the system blank. The PBM traps and denuders were then cooled by a cooling fan in the third step.

ACPD
14, 11041–11074, 2014

Four sampling campaigns were carried out for PBM and GOM measurements: 17 January–1 February, 8–18 May, 10–25 July, and 28 October to 11 November 2010. The selected periods represented four seasonal observations. Before sampling, the denuders were cleaned by pyrolysis to obtain the blank (1.67 ± 0.66 pg, N = 12). The quartz filter was cleaned by heating at 850 °C for 30 min. A somewhat higher blank (6.62 ± 2.69 pg, N = 20) was observed and used for correcting the PBM concentrations by subtracting the mean blank from the detected concentration.

2.3 Meteorological data and backward trajectory calculation

Meteorological parameters including hourly wind direction (WD), wind speed (WS), air temperature (AT), relative humidity (RH) and rainfall (RF) were continuously monitored by the SAWRS. The Indian monsoon indices (IMI), defined as the difference of 850 hPa zonal winds between a southern region of 5–15° N, 40–80° E and a northern region of 20–30° N, 70–90° E (Wang and Fan, 1999; Wang et al., 2001), were obtained online at the Asia-Pacific Air Data-Research Center (http://apdrc.soest.hawaii.edu/projects/monsoon/realtime-monidx.html). IMI reflects both the intensity of the tropical westerly monsoon and the lower-tropospheric vorticity anomalies associated with the ISM trough. Five-day backward trajectories were calculated using HYSPLIT (Wang et al., 2009; http://www.arl.noaa.gov/ready/hysplit4.html) to assess the long-range transport pathways. The Global Data Assimilation System (GDAS) meteorology archived by the Air Resource Laboratory of National Oceanic and Atmospheric Administration (NOAA) were used as the input (ftp://arlftp.arlhq.noaa.gov/pub/archives/gdas1/). The spatial and temporal resolution of the met data is 1° × 1° and 6 h, respectively. All back trajectories ended at the SAWRS (28°01′ N, 99°44′ E) at an arrival height of 500 m above ground. The back trajectories endpoints were recorded at 6 h intervals (02:00, 08:00, 14:00, 20:00 LT).

Cluster analysis was performed to obtain the synoptic transport pattern to the site. Clustering started by assigning each trajectory to its own cluster, so that there was the same number of clusters as the number of trajectories (i.e., one trajectory in each

ACPD
14, 11041–11074, 2014

cluster). For each iteration step, the cluster number was reduced by one as two clusters were merged together. For every combination of trajectory pairs, the cluster spatial variance (SV), defined as the sum of the squared distances between the endpoints of the cluster's component trajectories and the mean of the trajectories in that cluster, was computed. Then the total spatial variance (TSV), defined as the sum of all cluster SVs and increased for each additional inclusion of a trajectory, was calculated. The clustering process continued until the TSV suddenly increased by a large value, indicating that the included trajectory in the given iteration was not similar to the included trajectories included in a cluster. Such processes continued until the iterative step just before the large increase in the change of TSV gave the final number of clusters. Once the number of clusters was determined, the endpoints of trajectories in the same cluster were averaged and shown in the map.

Potential Source Contribution Function (PSCF) was performed to analyze and estimate the influence of the potential sources. The PSCF value for the ijth cell is then defined as:

The cluster spatial variance (CSV) was calculated as the sum of the spatial variance of all trajectories within its cluster and the total spatial variance (TSV) was calculated as the sum of the CSV over all clusters.

$$\mathrm{PSCF}_{ij} = \frac{M_{ij}}{N_{ij}} \quad (1)$$

Where M_{ij} represents the number of trajectory endpoints associated with 85 or higher percentiles of the observed TGM, N_{ij} is the number of endpoints associated with 50 or higher percentiles of the observed TGM. To reduce the effect of small values of N_{ij}, the PSCF values were multiplied by a weight function W_{ij} to reflect the uncertainty in the values for these cells (Polissar et al., 2001). The endpoints reaching the ground were excluded in the PSCF calculation. Overall, More than 27 000 endpoints were included

ACPD
14, 11041–11074, 2014

for the calculation. The weighting function was defined as:

$$W_{ij} = \begin{cases} 1.0 & n_{ij} > 3\text{Avg} \\ 0.7 & 1.5\text{Avg} < n_{ij} \le 3\text{Avg} \\ 0.4 & \text{Avg} < n_{ij} \le 1.5\text{Avg} \\ 0.2 & n_{ij} \le \text{Avg} \end{cases} \quad (2)$$

where Avg is the average endpoints in each grid cells.

3 Results and discussion

3.1 Distribution and influences of potential regional sources.

The 5 min time series plot of the observed TGM concentration is shown in Fig. 2. It ranged from 1.03 to 13.59 ng m^{-3} with a mean of 2.55 ± 0.73 ng m^{-3} (Table 1). Spikes of high TGM concentrations were observed from late April through early May, from late June through early July and in late September. The three high TGM periods occurred during the months when the ISM was prevailing, suggesting the ISM played an important role in the high TGM observed at the SAWRS (more in Sect. 3.3). The mean TGM level at the SAWRS were much lower than those observed in southwestern Chinese cities (9.7 ± 10.2 ng m^{-3} in Guiyang, Fu et al., 2011); 6.74 ± 0.37 ng m^{-3} in Chongqing, Yang et al., 2009). It was also lower than the background concentrations observed at Mt. Leigong in Guizhou province (2.80 ± 1.51 ng m^{-3}, Fu et al., 2010) and Mt. Gongga in Sichuan province (3.98 ± 1.62 ng m^{-3}, Fu et al., 2008), but higher than those observed at Mt. Changbai (1.60 ± 0.51 ng m^{-3}) in Northeast China and at Mt. Waliguan (WLG) Baseline Observatory (1.98 ± 0.98 ng m^{-3}) in Tibetan Plateau (Fu et al., 2012a). The TGM mean concentration at the SAWRS was slightly higher than the global background (1.5–1.7 ng m^{-3} in the Northern Hemisphere and 1.1–1.3 ng m^{-3} in the Southern Hemisphere, Lindberg et al., 2007). As a remote background site, the TGM level can only

ACPD
14, 11041–11074, 2014

be caused by long-range transport and possibly the weak local sources. Shangri-La is located between East Asia and South Asia, both have large regional Hg emissions (Fig. 1). Due to the nearby emission sources and the prevailing westerly, the TGM concentrations measured at in Korean and Japanese background sites were comparably higher (4.61 ng m^{-3} at Global Atmospheric Watch Station in An-Myun Island of Korea, Nguyen et al., 2007); 2.04 ng m^{-3} at Cape Hedo Station in Okinawa Island of Japan, Jaffe et al. (2005). The TGM concentration was lower at the background sites in North America and Europe (1.4–1.8 ng m^{-3} at Mace Head and Zingst of America, Kock et al., 2005). The elevated background level of TGM at the SAWRS is likely caused by the high regional sources in Asia.

The measured TGM concentration exhibited a strong dependence on wind direction. Higher TGM levels (2.5–2.7 ng m^{-3}) were frequently associated with northerly winds that carried domestic emissions from West China to the site (Fig. 3). The elevated TGM associated with the southerly winds could be caused by a combination of the regional emission sources in South Asia and the weak emission in the Shangri-La County in the south of the monitoring site. The wind flows from the east and west gave low TGM concentrations. The mountain ranges in Shangri-La area run in the north-south direction. The air masses in the east-west direction needed to cross high mountains to reach the SAWRS and therefore gave lower TGM concentrations. Figure 5 displays the diurnal trend of WD and WS along with those of TGM, GOM and PBM. The WD was predominantly southerly and transitioned from southeast (daytime) to southwest (nighttime). WS and TGM were slightly higher in daytime compared to those in nighttime. Since the SAWRS is located at a small mountaintop in Hengduan Mountain area, the terrain could affect local air circulation. The diurnal mountain valley breezes played a significant role in the vertical mixing. During daytime, air near mountaintop heats up faster than the air at the low altitude. The air mass rapidly rose and brought the Hg trapped in the boundary layer to the monitoring site. At nighttime, the cool air from the high mountains sank and carried the clean air from higher altitude to the site.

ACPD
14, 11041–11074, 2014

The diurnal pattern of GOM at the SAWRS showed higher concentrations in the afternoon. A possible reason is the lower relative humidity in air during the afternoon hours, which decreases the scavenging of GOM into droplets. Another possibility is the oxidation of Hg^0 caused by the stronger solar radiation (Lindberg et al., 2002; Goodsite et al., 2004). The measured PBM did not show a distinct diurnal trend. The observed diurnal pattern of TGM and GOM reflected the influence from local meteorology and from the photochemical productions.

3.2 Seasonal patterns of TGM, GOM and PBM

The seasonal statistics of the measured TGM, GOM, PBM, WS, AT, RH and RF are shown in Table 1. The TGM concentration in winter was lower (2.28 $ng\,m^{-3}$) compared to the level in the other three seasons. Temperature, RH and RF were also generally lower in winter after the retreat of the ISM. During the period, dry air masses, typically associated with high WS, from Tibetan Plateau caused the lower observed TGM. The TGM level was highest in spring (2.76 $ng\,m^{-3}$) and peaked in late April (Fig. 2) when RF, AT and RH increased with the onset of the ISM. The high TGM events were caused by the regional transport from the heavily industrial regions in Northwest China (more details in Sect. 3.3), with a peak observed concentration of 13.59 $ng\,m^{-3}$. Elevated TGM (2.71 $ng\,m^{-3}$) was also observed in autumn (Fig. 2), which was associated with lower AT, RH and RF. During the ISM period, the mean TGM level was 2.51 $ng\,m^{-3}$ despite the higher RH and RF.

The variation of the monthly means of TGM, WS, AT and RH is shown in Fig. 5. During the ISM season (May to September), a general negative correlation between mean TGM concentration and the RH/AT were evident. The higher RH in the summer months might have caused the lower concentration in those months. The gradual decrease of TGM concentration from May through August might also reflect the enhanced Hg uptake by vegetation, which has been observed several earlier study in Chang-Bai Mountain and in the Northeast US (Fu et al., 2012b; Obrist et al., 2008). The TGM concentration in the late autumn and winter months were also comparatively lower than

ACPD
14, 11041–11074, 2014

other months (except August) due to the more stagnant winds that limited the regional transport. The monthly variability in local WS was not substantial during the campaign and not likely to cause the observed seasonal variation.

Both GOM (Fig. 6a) and PBM (Fig. 6b) exhibited substantial seasonal variability. The GOM concentrations (mean: $7.90 \pm 7.89\,\mathrm{pg\,m^{-3}}$) were higher in autumn and peaked in winter ($15.72\,\mathrm{pg\,m^{-3}}$), about 5 times of the level in spring ($2.82\,\mathrm{pg\,m^{-3}}$). Similar pattern was observed at Storm Peak Laboratory (3220 m a.s.l.) in the Rocky Mountains of USA (Faïn et al., 2009). The elevated GOM has been attributed to the much lower RH, which was also the case at the SAWRS. Significant negative correlation ($r = -0.834$, $p < 0.001$) between GOM and RH concentrations was observed. The PBM concentrations (mean: $37.78 \pm 31.35\,\mathrm{pg\,m^{-3}}$) were high in autumn and winter, with a peak concentration at $58.60\,\mathrm{pg\,m^{-3}}$. In the absence of volcanic sources, PBM concentrations are usually associated with Hg emission from biomass burning and natural processing (Friedli et al., 2003; Finley et al., 2009). Trajectories analysis suggested that the high PBM during the campaign was associated with the air mass from Burma, Vietnam, Laos, Kampuchea and Thailand, likely of biomass burning origins. The PBM level was low from late spring to summer, possibly due to a greater degree of scavenging in the wet ISM period. The observed PBM and GOM also showed a negative correlation with RF ($r = -0.142$ and -0.186, respectively), indicating the scavenging of PBM and GOM by precipitation.

3.3 Air mass back trajectories analysis

Figure 7 shows the time series of WD, RF and TGM along with the calculated Indian Monsoon Index (IMI) during the possible ISM months (April through September). The values IMI represent seasonal rainfall anomalies, and are highly correlated with the transport associated with ISM (Wang et al., 2001). An IMI value > 0 suggests air transport from the south. Such a transport pattern was consistent from late May through mid-September. The period was also associated with higher RF caused by the moisture carried by the ISM. During this period, WD was mainly from the southeast. The

ACPD
14, 11041–11074, 2014

three high Hg events in Fig. 7 were further analyzed with the back trajectories of the air masses.

Figure 8 shows the back trajectories during 26 April to 2 May (first block in Fig. 7). The air masses originated from Siberia moved over north Xinjiang, east Qinghai, Gansu and west Sichuan provinces. These are industrial areas in Northwest China that have major Hg emission sources (Fig. 1), mainly from the use of fossil fuels (Wang et al., 2000; Fu et al., 2008, 2012a, c). From 19 June to 2 July (second block in Fig. 7), the air mass was mainly from the Bengal and Burma because of the ISM (Fig. 9), suggesting trans-boundary transport possibly caused by biomass burning in the region and the industrial cities (Fig. 1) such as Yangon (Burma's capital), Bangkok (Thailand's capital). Figure 1 shows the back trajectories during 17–22 September (third block in Fig. 7). Most trajectories in this period were very short and reached ground level (the endpoints were not shown after grounding). The elevated concentration in this event was likely to be contributed by the domestic emissions.

3.4 Cluster analysis of back trajectories

The back trajectories arriving at the SAWRS over the study period were grouped into four clusters (Fig. 11) to understand the regional transport pathways. Cluster 1 (19 %) represented air masses originating from North Africa and Siberia, passing through Middle Asia and then over Xinjiang, Qinghai provinces and Tibet of China. Cluster 2 (18 %) and Cluster 3 (59 %) were the air masses originating from South Asia and north India. Cluster 4, although relatively infrequent (4 %), was associated with the highest TGM concentrations (mean = 3.9 ng m^{-3}) due to the passing of air masses over known source regions in Sichuan province. The area has a high background TGM level (3.98 ng m^{-3}) caused by industrial and domestic coal combustion, smelting industries, cement production, and biomass burning (Fu et al., 2008). Air masses of Cluster 3, the most frequent transport sector, also had high TGM concentrations (mean = 2.6 ng m^{-3}). The most likely source region was South Asia's biomass burning activities. TGM concentration (2.4 ng m^{-3}) associated with Cluster 2, also in frequent, could be linked to

ACPD
14, 11041–11074, 2014

transport of atmospheric Hg from Pakistan and northern India including New Delhi. Anthropogenic Hg emission in India has drawn increasing attention in recent years (Qureshi et al., 2013). Air masses in Cluster 1 showed the lowest mean TGM concentration (2.3 ng m^{-3}) and originated from the west Asia. This cluster was also associated with high wind speed caused by the strong prevailing westerly in cold season.

The back trajectories of the upper quartile of TGM observations at the SAWRS were displayed in Fig. 12. It is clear that the frequent transport from South and Southeast Asia during summer and autumn dominated the high TGM observation at the SAWRS. The winter and spring trajectories originated from Siberia, North Africa and Mediterranean and then passed through Middle East and Tibetan Plateau were more likely caused by the domestic sources in China. The relatively shorter trajectories from South Asia suggest that the transport from this sector may be caused by mild air movement of the ISM (summer and early autumn). The back trajectories associated with the lower quartile of TGM observations were comparatively longer and from random directions, suggesting the effect caused by meteorology (Fig. 13).

The potential sources and transport pathways of TGM at the SAWRS is shown in Fig. 14 as a PSCF distribution plot. It suggests that Burma, Bengal bay, north India, west Sichuan Province and west Yunnan Province were likely the source regions. Trans-boundary transport of aerosols released from forest fires and agricultural burning in the Bengal bay region had been attributed to the seasonal changes of air movement caused by monsoons (Reid et al., 2013). Our PSCF analysis seems to support such trans-boundary transport events. Two high PSCF values in India were also identified, including the surrounding areas of New Delhi and Uttar Pradesh. Both are considered large urban regions with high industrial activities. Domestic source regions in Sichuan and Yunnan were also identified. The atmospheric mercury concentrations observed at the SAWRS were influenced by both domestic and foreign emission sources and highly dependent on the seasonal winds that carry the air masses from different source regions to the observational site.

ACPD
14, 11041–11074, 2014

4 Conclusions

Ambient measurements of TGM, GOM and PBM from November 2009 to November 2010 at the SAWRS, a high-elevation background site in Tibetan Plateau of China, were investigated. The mean TGM (2.55 ng m^{-3}) was higher than the background values observed in the Northern Hemisphere (1.5–2.0 ng m^{-3}). Significant seasonal variability in TGM concentration was observed. The seasonal variation was attributed to meteorological factors and long-range transport caused by the ISM and westerlies. The ISM enhanced TGM concentration occasionally by carrying Hg-enriched air caused by biomass burning in South Asia to the SAWRS, while the moist air carried by the ISM significantly decreased GOM and PBM level. The westerlies carried the Hg emission from the domestic sources in China to the site. The TGM concentration was higher during the daytime mainly due to the diurnal surface temperature shift. High GOM levels were correlated with dry air in autumn and winter, and the in-situ photochemical productions of might have contributed to the occasional high GOM concentrations. Back trajectory analysis showed that the SAWRS was strongly affected by ISM and westerlies during the campaign period, which carried Hg-enriched air masses to the site from South Asia and industrial regions in China in different seasons.

Acknowledgements. This work is supported by National "973" Program (2013CB430003), Natural Science Foundation of China (41273145, 41173024), and State Key Laboratory of Environmental Geochemistry. We also thank the staff of Meteorological Bureau of Diqing Tibetan Autonomous Prefecture for field sampling assistance.

References

Carpi, A. and Lindberg, S. E.: Application of a Teflon (TM) dynamic flux chamber for quantifying soil mercury flux: tests and results over background soil, Atmos. Environ., 32, 873–882, 1998.

ACPD
14, 11041–11074, 2014

Driscoll, C. T., Mason, R. P., Chan, H. M., Jacob, D. J., and Pirrone, N.: Mercury as a global pollutant: sources, pathways, and effects, Environ. Sci. Technol., 47, 4967–4983, doi:10.1021/es305071v, 2013.

Faïn, X., Obrist, D., Hallar, A. G., Mccubbin, I., and Rahn, T.: High levels of reactive gaseous mercury observed at a high elevation research laboratory in the Rocky Mountains, Atmos. Chem. Phys., 9, 8049–8060, doi:10.5194/acp-9-8049-2009, 2009.

Feng, X., Sommar, J., Gårdfeldt, K., and Lindqvist, O.: Improved determination of gaseous divalent mercury in ambient air using KCl coated denuders, Fresen. J. Anal. Chem., 366, 423–428, 2000.

Finley, B., Swartzendruber, P., and Jaffe, D.: Particulate mercury emissions in regional wildfire plumes observed at the Mount Bachelor Observatory, Atmos. Environ., 43, 6074–6083, 2009.

Friedli, H., Radke, L., Prescott, R., Hobbs, P., and Sinha, P.: Mercury emissions from the August 2001 wildfires in Washington State and an agricultural waste fire in Oregon and atmospheric mercury budget estimates, Global Biogeochem. Cy., 17, 1039, doi:10.1029/2002GB001972, 2003.

Fu, X., Feng, X., Zhu, W., Wang, S., and Lu, J.: Total gaseous mercury concentrations in ambient air in the eastern slope of Mt. Gongga, South-Eastern fringe of the Tibetan Plateau, China, Atmos. Environ., 42, 970–979, 2008.

Fu, X., Feng, X., Dong, Z. Q., Yin, R. S., Wang, J. X., Yang, Z. R., and Zhang, H.: Atmospheric gaseous elemental mercury (GEM) concentrations and mercury depositions at a high-altitude mountain peak in south China, Atmos. Chem. Phys., 10, 2425–2437, doi:10.5194/acp-10-2425-2010, 2010.

Fu, X., Feng, X., Qiu, G., Shang, L., and Zhang, H.: Speciated atmospheric mercury and its potential source in Guiyang, China, Atmos. Environ., 45, 4205–4212, 2011.

Fu, X., Feng, X., Liang, P., Deliger, Zhang, H., Ji, J., and Liu, P.: Temporal trend and sources of speciated atmospheric mercury at Waliguan GAW station, Northwestern China, Atmos. Chem. Phys., 12, 1951–1964, doi:10.5194/acp-12-1951-2012, 2012a.

Fu, X., Feng, X., Shang, L. H., Wang, S. F., and Zhang, H.: Two years of measurements of atmospheric total gaseous mercury (TGM) at a remote site in Mt. Changbai area, Northeastern China, Atmos. Chem. Phys., 12, 4215–4226, doi:10.5194/acp-12-4215-2012, 2012b.

Fu, X., Feng, X., Sommar, J., and Wang, S.: A review of studies on atmospheric mercury in China, Sci. Total Environ., 421, 73–81, 2012c.

ACPD
14, 11041–11074, 2014

Gay, D. A., Schmeltz, D., Prestbo, E., Olson, M., Sharac, T., and Tordon, R.: The Atmospheric Mercury Network: measurement and initial examination of an ongoing atmospheric mercury record across North America, Atmos. Chem. Phys., 13, 11339–11349, doi:10.5194/acp-13-11339-2013, 2013.

Goodsite, M. E., Plane, J., and Skov, H.: A theoretical study of the oxidation of Hg^0 to $HgBr_2$ in the troposphere, Environ. Sci. Technol., 38, 1772–1776, 2004.

Iverfeldt, Å. and Lindqvist, O.: Atmospheric oxidation of elemental mercury by ozone in the aqueous phase, Atmos. Environ., 20, 1567–1573, 1986.

Jaffe, D., Prestbo, E., Swartzendruber, P., Weiss-Penzias, P., Kato, S., Takami, A., Hatakeyama, S., and Kajii, Y.: Export of atmospheric mercury from Asia, Atmos. Environ., 39, 3029–3038, 2005.

Johansson, K., Bergbäck, B., and Tyler, G.: Impact of atmospheric long range transport of lead, mercury and cadmium on the Swedish forest environment, Water Air Soil Poll.: Focus, 1, 279–297, 2001.

Kock, H., Bieber, E., Ebinghaus, R., Spain, T., and Thees, B.: Comparison of long-term trends and seasonal variations of atmospheric mercury concentrations at the two European coastal monitoring stations Mace Head, Ireland, and Zingst, Germany, Atmos. Environ., 39, 7549–7556, 2005.

Landis, M. S., Stevens, R. K., Schaedlich, F., and Prestbo, E. M.: Development and characterization of an annular denuder methodology for the measurement of divalent inorganic reactive gaseous mercury in ambient air, Environ. Sci. Technol., 36, 3000–3009, 2002.

Li, J. and Lee, S. M.: Progress of global atmospheric mercury field observations, J. Clean Energy Technologies, 2, 252–257, doi:10.7763/JOCET.2014.V2.135, 2014.

Lin, C. J. and Pehkonen, S. O.: The chemistry of atmospheric mercury: a review, Atmos. Environ., 33, 2067–2079, 1999.

Lindberg, S. E., Bullock, R., Ebinghaus, R., Engstrom, D., Feng, X., Fitzgerald, W., Pirrone, N., Prestbo, E., and Seigneur, C.: A synthesis of progress and uncertainties in attributing the sources of mercury in deposition, AMBIO: a Journal of the Human Environment, 36, 19–33, 2007.

Lindberg, S. E., Brooks, S., Lin, C.-J., Scott, K. J., Landis, M. S., Stevens, R. K., Goodsite, M., and Richter, A.: Dynamic oxidation of gaseous mercury in the Arctic troposphere at polar sunrise, Environ. Sci. Technol., 36, 1245–1256, 2002.

ACPD
14, 11041–11074, 2014

Lindqvist, O.: Mercury in the Swedish environment: recent research on causes, consequences and corrective methods, Water Air Soil Poll., 55, 1–261, 1991.
Loewen, M., Kang, S., Armstrong, D., Zhang, Q., Tomy, G., and Wang, F.: Atmospheric transport of mercury to the Tibetan Plateau, Environ. Sci. Technol., 41, 7632–7638, 2007.
Nguyen, H. T., Kim, K. H., Kim, M. Y., Hong, S., Youn, Y. H., Shon, Z. H., and Lee, J. S.: Monitoring of atmospheric mercury at a global atmospheric watch (GAW) site on An-Myun Island, Korea, Water Air Soil Poll., 185, 149–164, 2007.
Obrist, D., Hallar, A., McCubbin, I., Stephens, B. B., and Rahn, T.: Atmospheric mercury concentrations at Storm Peak Laboratory in the Rocky Mountains: evidence for long-range transport from Asia, boundary layer contributions, and plant mercury uptake, Atmos. Environ., 42, 7579–7589, 2008.
Pacyna, E. G., Pacyna, J. M., Steenhuisen, F., and Wilson, S.: Global anthropogenic mercury emission inventory for 2000, Atmos. Environ., 40, 4048–4063, 2006.
Pirrone, N., Keeler, G. J., and Nriagu, J. O.: Regional differences in worldwide emissions of mercury to the atmosphere, Atmos. Environ., 30, 2981–2987, 1996.
Pirrone, N., Costa, P., Pacyna, J., and Ferrara, R.: Mercury emissions to the atmosphere from natural and anthropogenic sources in the Mediterranean region, Atmos. Environ., 35, 2997–3006, 2001.
Pirrone, N., Cinnirella, S., Feng, X., Finkelman, R. B., Friedli, H. R., Leaner, J., Mason, R., Mukherjee, A. B., Stracher, G. B., Streets, D. G., and Telmer, K.: Global mercury emissions to the atmosphere from anthropogenic and natural sources, Atmos. Chem. Phys., 10, 5951–5964, doi:10.5194/acp-10-5951-2010, 2010.
Polissar, A. V., Hopke, P. K., and Harris, J. M.: Source regions for atmospheric aerosol measured at Barrow, Alaska, Environ. Sci. Technol., 35, 4214–4226, 2001.
Qureshi, A., Vadenbo, C., and Hellweg, S.: Anthropogenic mercury flows in India and impacts of emission controls, Environ. Sci. Technol., 47, 8105–8113, doi:10.1021/es401006k, 2013.
Reid, J. S., Hyer, E. J., Johnson, R. S., Holben, B. N., Yokelson, R. J., Zhang, J., Campbell, J. R., Christopher, S. A., Di Girolamo, L., and Giglio, L.: Observing and understanding the Southeast Asian aerosol system by remote sensing: an initial review and analysis for the Seven Southeast Asian Studies (7SEAS) program, Atmos. Res., 122, 403–468, 2013.
Schroeder, W. H., Keeler, G., Kock, H., Roussel, P., Schneeberger, D., and Schaedlich, F.: International field intercomparison of atmospheric mercury measurement methods, Water Air Soil Poll., 80, 611–620, 1995.

ACPD
14, 11041–11074, 2014

Schroeder, W. H. and Munthe, J.: Atmospheric mercury-an overview, Atmos. Environ., 32, 809–822, 1998.
Sharma, D. C.: Concern over mercury pollution in India, Lancet, 362, 1050, doi:10.1016/S0140-6736(03)14456-X, 2003.
Sprovieri, F., Gratz, L., and Pirrone, N.: Development of a Ground-Based Atmospheric Monitoring Network for the Global Mercury Observation System (GMOS), E3S Web of Conferences, 17007, Rome, Italy, 22–27 September 2012, doi:10.1051/e3sconf/20130117007, 2013.
Streets, D. G., Hao, J., Wu, Y., Jiang, J., Chan, M., Tian, H., and Feng, X.: Anthropogenic mercury emissions in China, Atmos. Environ., 39, 7789–7806, 2005.
Sunderland, E. M., Krabbenhoft, D. P., Moreau, J. W., Strode, S. A., and Landing, W. M.: Mercury sources, distribution, and bioavailability in the North Pacific Ocean: insights from data and models, Global Biogeochem. Cy., 23, GB2010, doi:10.1029/2008GB003425, 2009.
Valente, R. J., Shea, C., Lynn Humes, K., and Tanner, R. L.: Atmospheric mercury in the Great Smoky Mountains compared to regional and global levels, Atmos. Environ., 41, 1861–1873, 2007.
Wang, B. and Fan, Z.: Choice of South Asian summer monsoon indices, B. Am. Meteorol. Soc., 80, 629–638, 1999.
Wang, B., Wu, R., and Lau, K.: Interannual Variability of the Asian Summer Monsoon: contrasts between the Indian and the western North Pacific–East Asian Monsoons*, J. Climate, 14, 4073–4090, 2001.
Wang, Q., Shen, W., and Ma, Z.: Estimation of mercury emission from coal combustion in China, Environ. Sci. Technol., 34, 2711–2713, 2000.
Xiao, Z., Sommar, J., Wei, S., and Lindqvist, O.: Sampling and determination of gas phase divalent mercury in the air using a KCl coated denuder, Fresen. J. Anal. Chem., 358, 386–391, 1997.
Xu, B., Cao, J., Hansen, J., Yao, T., Joswia, D. R., Wang, N., Wu, G., Wang, M., Zhao, H., and Yang, W.: Black soot and the survival of Tibetan glaciers, P. Natl. Acad. Sci. USA, 106, 22114–22118, 2009.
Yang, Y., Chen, H., and Wang, D.: Spatial and temporal distribution of gaseous elemental mercury in Chongqing, China, Environ. Monit. Assess., 156, 479–489, 2009.
Zhang, Q., Huang, J., Wang, F., Mark, L., Xu, J., Armstrong, D., Li, C., Zhang, Y., and Kang, S.: Mercury Distribution and Deposition in Glacier Snow over Western China, Environ. Sci. Technol., 46, 5404–5413, 2012.

ACPD
14, 11041–11074, 2014

Table 1. The seasonal statistics of the measured TGM, GOM, PBM, WS, AT, RH and RF from November 2009 through November 2010 at the SAWRS site.

		TGM ($ng\,m^{-3}$)	GOM ($pg\,m^{-3}$)	PBM ($pg\,m^{-3}$)	AT (°C)	RH (%)	WS ($m\,s^{-1}$)	RF (mm)
Spring	Mean	2.76	2.82	32.82	4.85	78.06	1.98	34.07
Mar–May	± St.Dev	0.87	3.18	25.24	3.32	12.88	0.63	
	Median	2.6	1.05	26.93	4.05	79.5	1.9	
	Range	1.43–13.59	0.33–16.69	0.48–112.82	−0.4–13	37–98	0.7–3.4	
Summer	Mean	2.51	3.79	25.46	12.37	85.97	1.63	183.97
Jun–Aug	± St.Dev	0.71	3.80	18.37	1.59	7.91	0.61	
	Median	2.35	2.8	22.14	12.4	87	1.5	
	Range	1.05–6.11	0.24–18.81	1.50–86.97	7.2–15.6	65–99	0.5–3.4	
Autumn	Mean	2.71	7.46	59.14	6.25	84.46	1.5	38.17
Sep–Nov	± St.Dev	0.79	6.18	39.31	3.61	8.39	0.44	
	Median	2.59	5.23	45.83	6.3	84.5	1.5	
	Range	1.03–6.99	0.44–31.09	10.93–185.06	−0.3–11.7	63–99	0.4–2.66	
Winter	Mean	2.28	14.48	21.22	−1.37	54.68	2.34	0
Dec–Feb	± St.Dev	0.42	9.18	15.86	1.64	16.98	0.72	
	Median	2.22	12.66	15.23	−1.11	58	2.25	
	Range	1.18–4.51	0.6–39.85	2.01–65.9	−6.6–1.6	19–84	0.9–4.3	
Total	Mean	2.55	7.90	37.78	5.57	75.97	1.86	
	± St.Dev	0.73	7.89	31.35	5.57	16.81	0.68	
	Median	2.39	4.78	30.42	5.1	7 9	1.8	
	Range	1.03–13.59	0.24–39.85	0.48–185.59	−6.6–15.6	19–99	0.4–4.3	

ACPD
14, 11041–11074, 2014

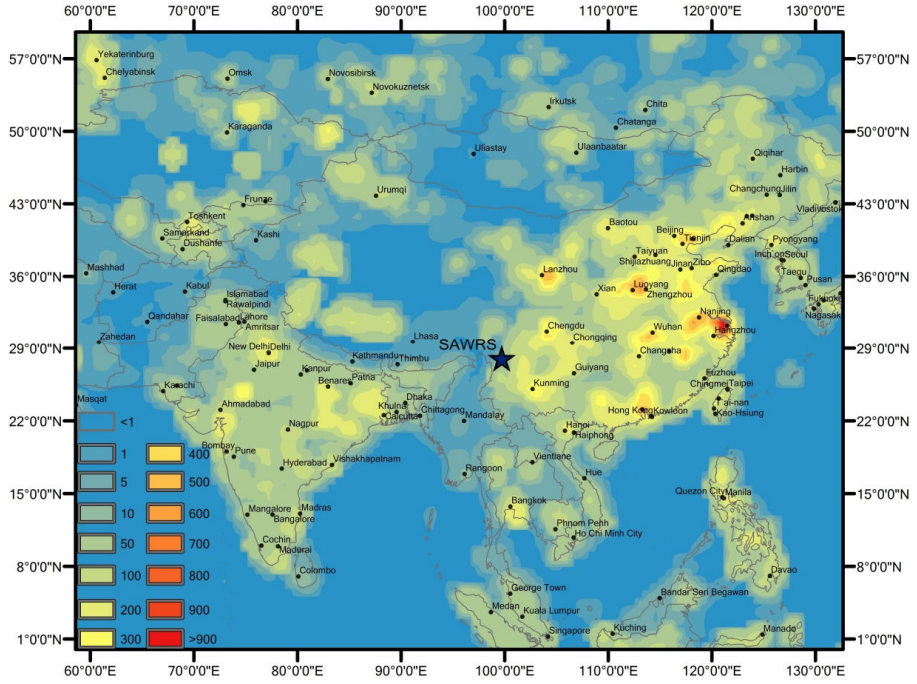

Fig. 1. The location of SAWRS, anthropogenic Hg emissions ($g\,km^{-2}$) and big cities in Asia where have a large number of population and industrial production.

ACPD
14, 11041–11074, 2014

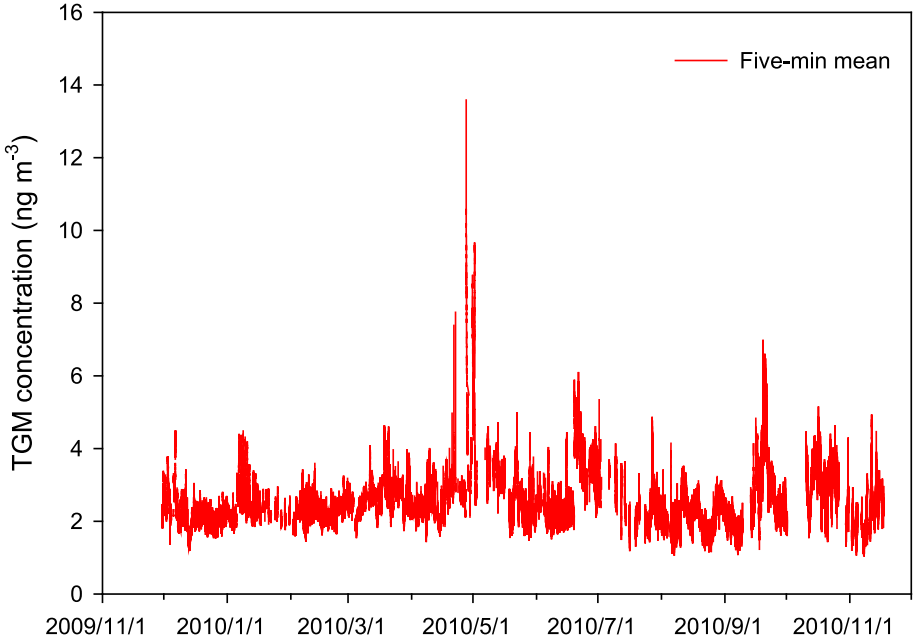

Fig. 2. The 5 min time series distribution of TGM concentrations at SAWRS in the campaign, spikes of high TGM concentrations were observed from late April through early May, from late June through early July and in late September, respectively.

ACPD
14, 11041–11074, 2014

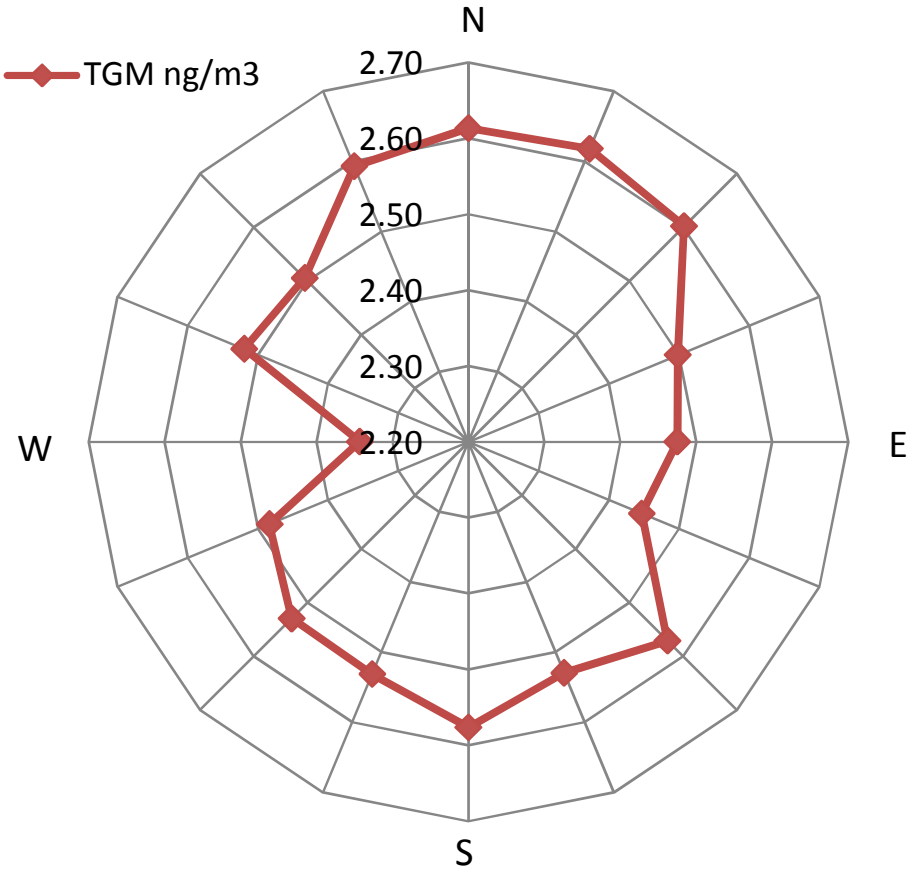

Fig. 3. The concentration wind roses at SAWRS, TGM concentration exhibited a strong dependence on wind direction. Higher TGM levels were frequently associated with northerly winds.

ACPD
14, 11041–11074, 2014

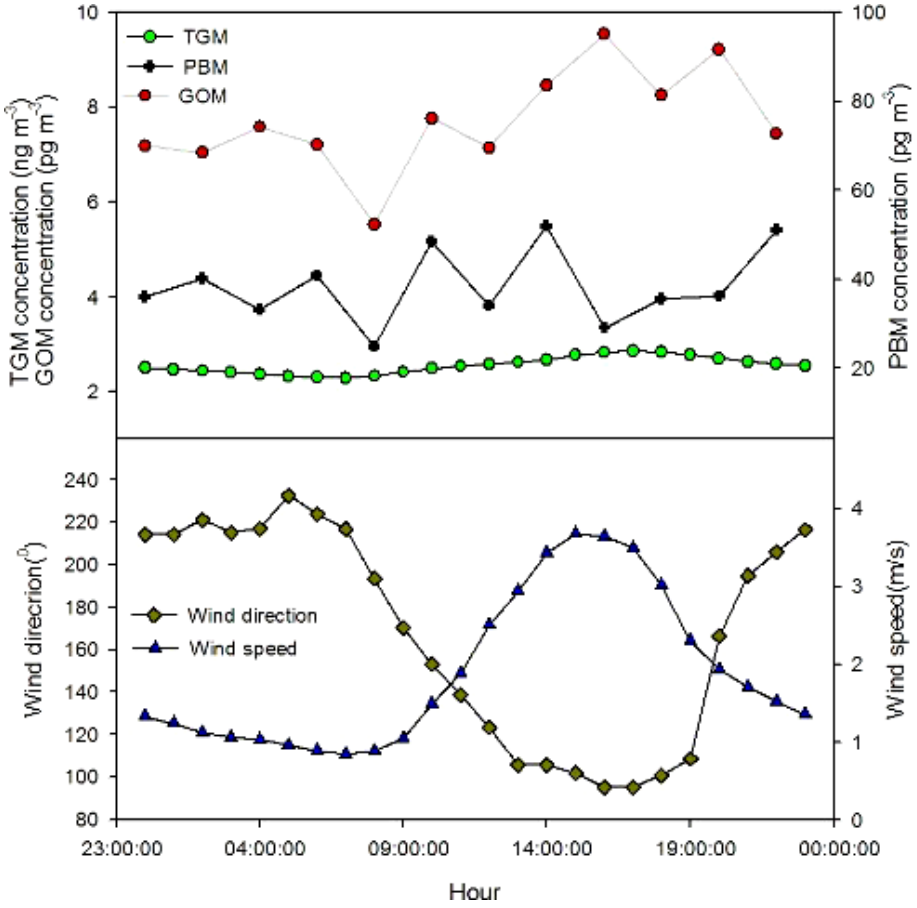

Fig. 4. The diurnal variation of TGM, GOM and PBM with WD and WS. The diurnal pattern of TGM and GOM at the SAWRS was typically higher in the afternoon. The measured PBM did not show any distinct trend.

ACPD
14, 11041–11074, 2014

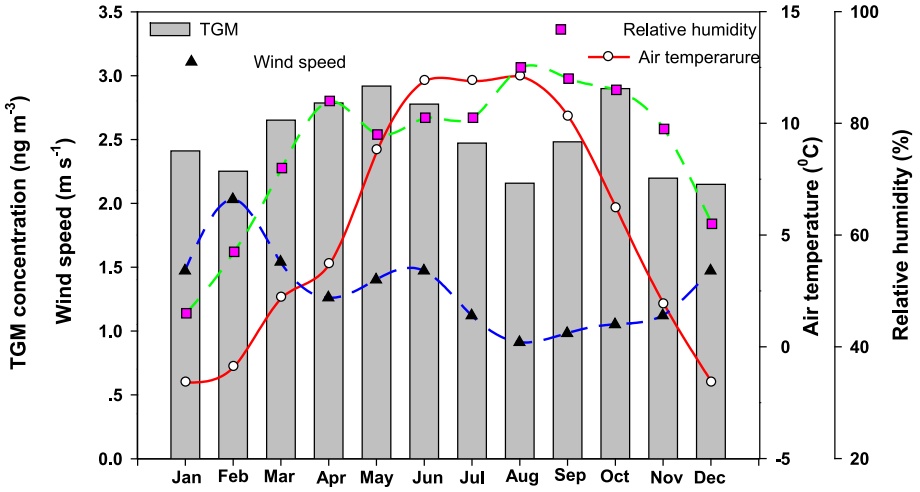

Fig. 5. The variation of the monthly means of TGM, WS, AT and RH. High TGM concentration in ISM period with high AT and RH. The TGM concentration in the late autumn and winter months were also comparatively lower than other months.

ACPD
14, 11041–11074, 2014

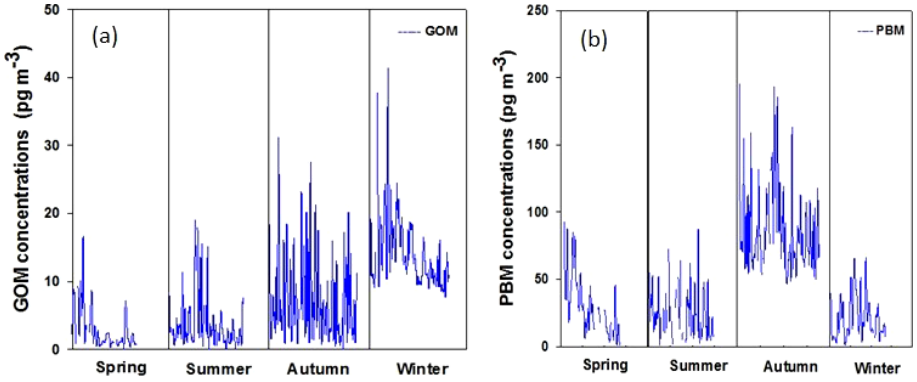

Fig. 6. Seasonal variability of GOM and PBM during four sampling campaigns. GOM concentrations were higher in autumn and winter than in other seasons with the highest GOM concentrations in winter **(a)**. PBM concentrations showed the highest level in autumn but very low in winter **(b)**.

ACPD
14, 11041–11074, 2014

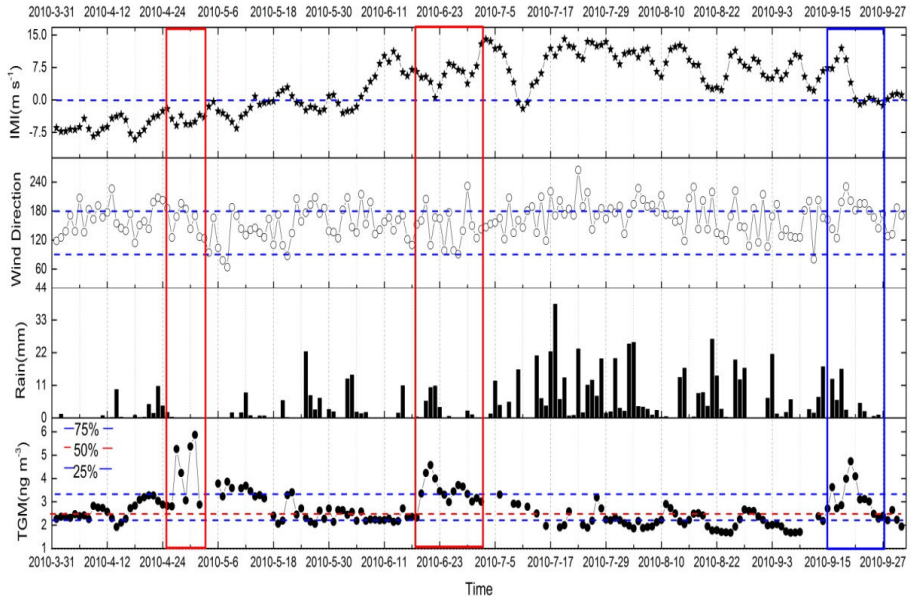

Fig. 7. Time series of WD, RF and TGM and the calculated Indian Monsoon Index (IMI) from April to September 2010. An IMI value > 0 indicates air movement from south toward north, which is also associated with greater precipitation. WD measured at the SAWRS was mostly from the southeast.

ACPD
14, 11041–11074, 2014

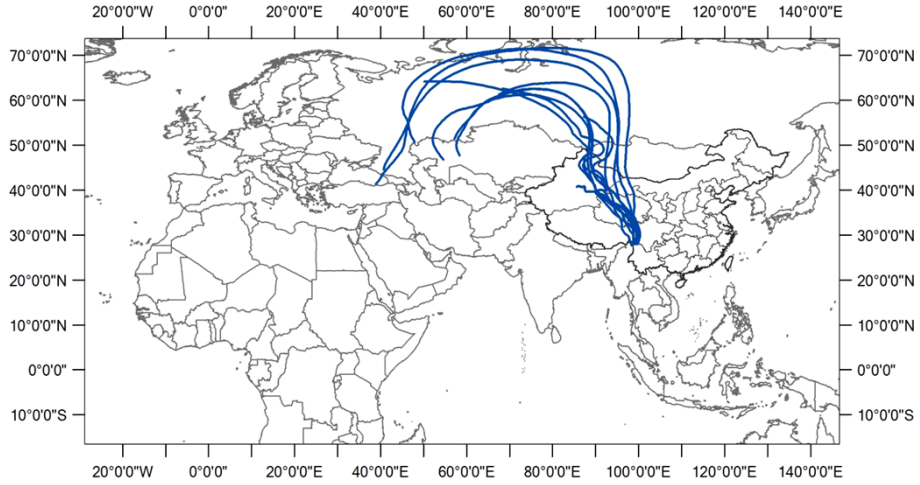

Fig. 8. The back trajectories of air mass from 26 April to 2 May. The air mass originated from Siberia moved over northern Xinjiang, east Qinghai, Gansu and west Sichuan province that have major points sources.

ACPD
14, 11041–11074, 2014

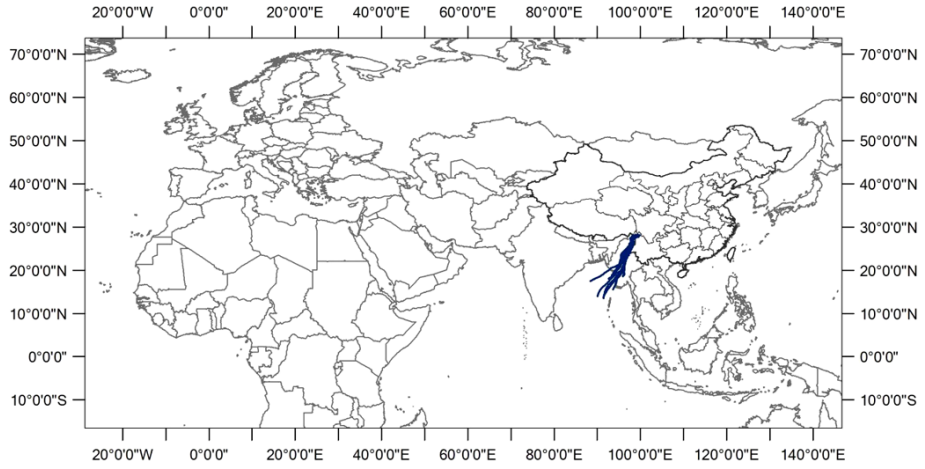

Fig. 9. The back trajectories of air mass from 19 June to 2 July. The air mass was mainly from the Bengal and Burma because of the ISM.

ACPD
14, 11041–11074, 2014

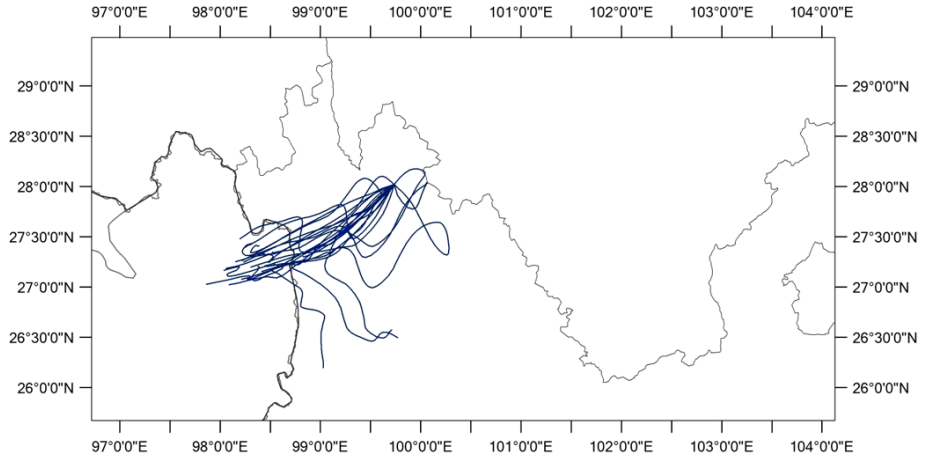

Fig. 10. The back trajectories of air mass from 17 to 22 September. The trajectory points reaching the ground level are not shown in the figure.

ACPD
14, 11041–11074, 2014

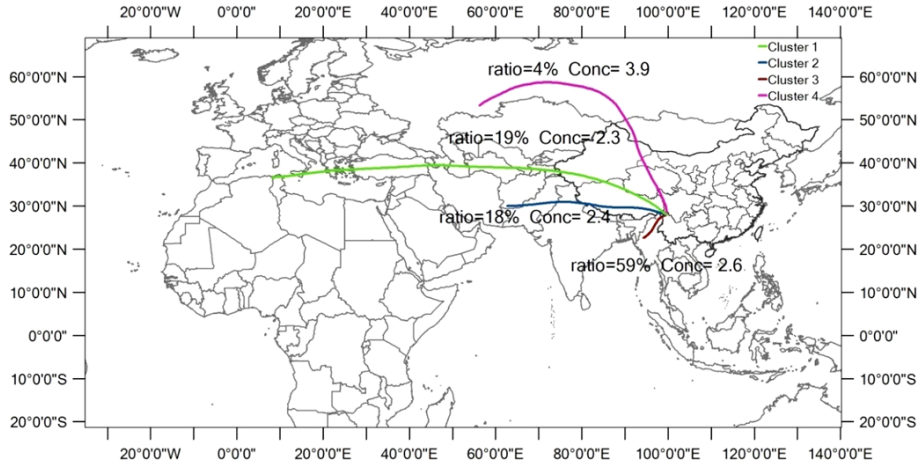

Fig. 11. The back trajectories arriving at the SAWRS over the study period were grouped into six clusters. Cluster 1 (19 %) and Cluster 4 (4 %) show that air masses originated from the west Asia and Middle East, passed over Middle Asia and then moved over Xinjiang, Qinghai province and Tibet of China. Cluster 2 (18 %) and Cluster 3 (59 %) show consists of air masses originating from Southeast Asia and north India.

ACPD
14, 11041–11074, 2014

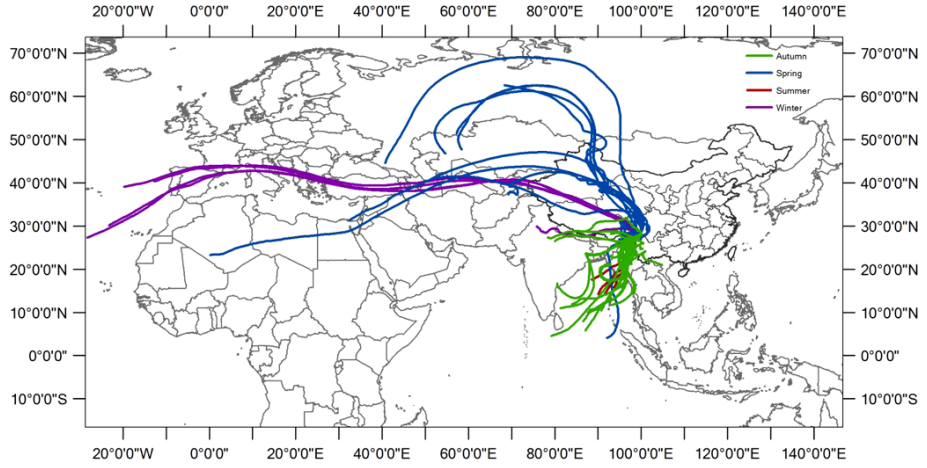

Fig. 12. The back trajectories of the upper quartile of TGM observations at the SAWRS. The air masses with high Hg were from South and Southeast Asia in autumn and winter. The air masses were from west Asia, Middle Asia and Tibetan Plateau.

ACPD
14, 11041–11074, 2014

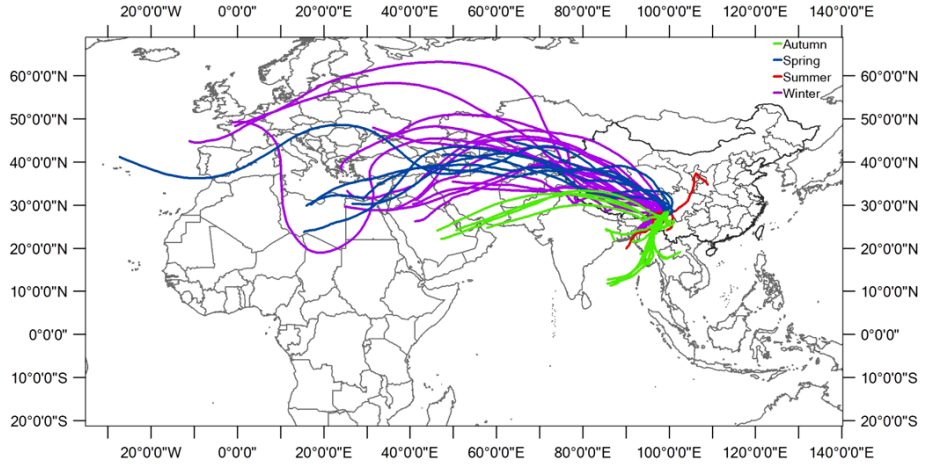

Fig. 13. The back trajectories associated with the lower quartile of TGM observations were comparatively longer and from random directions.

ACPD
14, 11041–11074, 2014

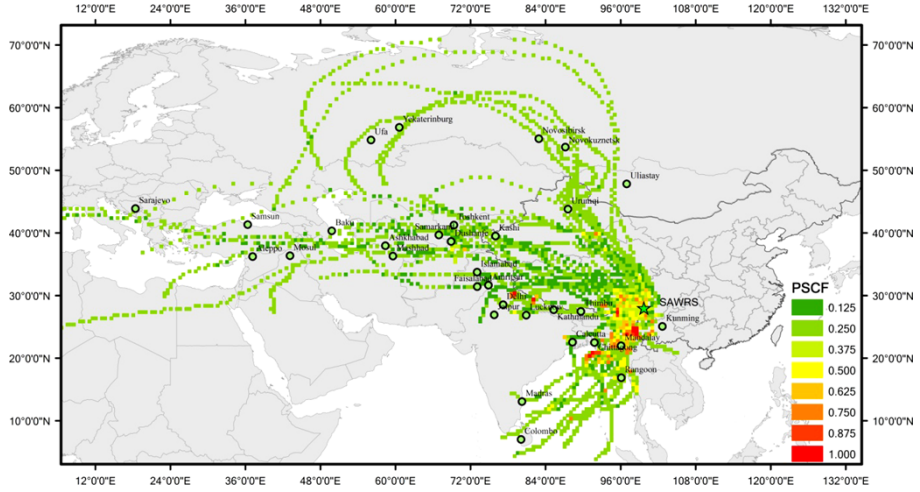

Fig. 14. The potential sources and transport pathways of TGM at the SAWRS at SAWRS identified by the PSCF. Burma, Bengal bay, north India, western Sichuan Province and western Yunnan Province were likely the potential source regions for Shangri-La.

ACPD
14, 11041–11074, 2014